Journal of Materials Chemistry C

ROYAL SOCIETY OF CHEMISTRY

PAPER

View Article Online
View Journal | View Issue

Cite this: J. Mater. Chem. C, 2022, 10, 13878

Semitransparent near-infrared Sn–Pb hybrid perovskite photodetectors

Arghanoon Moeini, † Laura Martínez-Sarti, † Kassio P. S. Zanoni, Michele Sessolo, Daniel Tordera * and Henk J. Bolink

Received 15th March 2022,
Accepted 10th May 2022

DOI: 10.1039/d2tc01052f

rsc.li/materials-c

Perovskite photodetectors are a promising technology for imaging applications, due to their high performance, tunable absorption spectrum and large area processability. New applications require devices with properties such as transparency, near-infrared (NIR) absorption or scalability. Here, we have fabricated semitransparent NIR perovskite photodetectors based on tin–lead (Sn–Pb) hybrid perovskites, by using very thin film perovskite layers (200 nm) and transparent indium tin oxide (ITO) electrodes. The top ITO contact was processed *via* pulsed layer deposition (PLD) with no damage to the underlying stack. The photodetectors have a full stack transmission of over 48% in the NIR (between 780 and 1100 nm) and exhibit good performance with a dark current of 1.74×10^{-2} mA cm^{-2} (at −0.2 V), external quantum efficiency of 23% and 13%, and detectivity of 6.6×10^{10} and 4.2×10^{10} Jones (at −0.2 V), at 850 and 940 nm, respectively. The performance of these devices makes them good candidates to be used as photodetectors for NIR applications or as bifacial devices.

Introduction

Photodetectors are the cornerstone of imaging technologies in fields like surveillance,[1] chemical sensing,[2] biomedicine,[3] and biometrics.[4] As these technologies evolve, so does the need for the design and fabrication of novel devices for new applications. For instance, near-infrared (NIR) photodetectors are required for applications such as vein recognition,[5] pulse oximetry,[6] brain imaging,[7] proximity sensors,[8] spectrometry for food monitoring[9] or skin cancer diagnosis.[10] Other applications require the integration of the imager in front of a display (such as phones, computers, or ATMs), where semitransparent devices are needed.[11] Semitransparent devices can be obtained *via* downscaling of the active area (*e.g.* by photolithography),[12] by using materials that are transparent in the visible spectrum (narrow bandgap semiconductors)[13–15] or by using very thin semiconductors in combination with transparent electrodes, such as transparent conducting oxides (TCOs), graphene, organic or nanostructured electrodes.[15,16] For many applications, large-area cost-efficient processing is also preferred. Scaling up silicon-based photodetectors has proven to be difficult but materials such as (semi-)conducting polymers, quantum dots, or perovskites, have already been processed into large-area devices.[17–19] For certain applications, like the use of biometric vein detection imagers integrated in consumer electronics, the combination of these three features is required: NIR sensitivity, semitransparency, and large-area sensing.[20]

Metal halide perovskites (hereinafter referred to as perovskites) are crystalline materials with the chemical structure AMX_3, where A is a monovalent cation (such as methylammonium, MA^+, or cesium, Cs^+), B is a divalent metal (typically Pb^{2+} or Sn^{2+}), and X is a halide (Cl^-, Br^- or I^-).[21,22] Pb-based perovskites have excellent optoelectronic properties due to their

Instituto de Ciencia Molecular (ICMol), Universidad de Valencia, C/Catedrático J. Beltrán 2, 46980 Paterna (Valencia), Spain. E-mail: daniel.tordera@uv.es
† Authors contributed equally to this work.

Daniel Tordera

Daniel Tordera is an Assistant Professor at the Physical Chemistry Department and the Molecular Science Institute of the University of Valencia, where his research focuses on the topic of perovskite optoelectronic devices. He received his PhD in Nanotechnology at the University of Valencia in 2014. After that he followed a rather unorthodox path, starting his own spin-off (Lec-Val Lighting, 2014), going back to academia as a postdoc (Linköping University, 2015), and working as a researcher of industrial projects for high-tech companies (Holst Centre at TNO, 2017). When he is not at the lab he enjoys writing thrillers. His first novel "El arte de la fuga" was one of the ten finalists of the biggest award in Spanish language (Premio Planeta) and has been published this year.

high charge carrier mobility, large light absorption coefficient, long diffusion length and high resilience to defects.[23] For these reasons, they have extensively been used as the active materials in solar cells,[24,25] exhibiting record power conversion efficiencies of up to 25.6% in single-junction cells,[26] and more recently in photodetectors.[27] In particular, the most extensively investigated perovskite used in solar cells, methylammonium lead iodide ($MAPbI_3$), has been also widely used as the active material for photodiodes.[27] However, $MAPbI_3$ has a bandgap of approximately 1.6 eV with an absorption edge close to 800 nm,[28] which limits its spectral response to the visible spectrum. Other frequently used Pb-based perovskites (such as $CsPbBr_3$) are also limited to this region of the electromagnetic spectrum.[29] In order to extend the absorption to longer wavelengths, different strategies have been adopted such as combining $MAPbI_3$ perovskites with quantum dots,[30,31] using tin (Sn)-based perovskites[32] or, more commonly, by alloying Sn and Pb in mixed metal perovskites.[33,34] Sn–Pb hybrid perovskites can have a bandgap as low as 1.17 eV, showing a broadband absorption from the visible to the NIR (up to *ca.* 1050 nm).[35–37] Regarding transparency, semitransparent perovskite photodetectors are also being widely investigated, as shown by the sheer amount of published work in the recent years.[38,39] However, most of the examples found in the literature focus solely on the visible spectral range. An exception to this is the work of Zhu *et al.* who, in 2020, developed a bilayer perovskite/PbSe quantum dots structure that, combined with transparent polymeric electrodes, resulted in semitransparent photodetectors capable to absorb from the visible well into the NIR region, *via* the trap-assisted photomultiplication effect.[40] Therefore, the development of novel semitransparent NIR perovskite photodetectors is still an unexplored field of research, in particular devices with a simple architecture yet delivering a good performance.

In this work we demonstrate, to the best of our knowledge, the first semitransparent NIR perovskite photodetector employing mixed Sn–Pb perovskite as the active material. The devices consist of a methylammonium (MA^+) formamidinium (FA^+) tin lead iodide ($MA_{0.3}FA_{0.7}Pb_{0.5}Sn_{0.5}I_3$) perovskite active layer sandwiched between two transparent indium tin oxide (ITO) electrodes. The top electrode was processed *via* pulsed layer deposition (PLD) with no observable damage to the underlying perovskite layer. The full device stack exhibits a transparency of over 48% in the NIR spectral region. The photodetectors present a dark current of 1.74×10^{-2} mA cm^{-2} (at -0.2 V), a broadband external quantum efficiency (EQE) that extends into the NIR ($\sim$1050 nm) with values of 23% and 13% for 850 and 940 nm, respectively, and high detectivity of 6.6×10^{10} and 4.2×10^{10} Jones for 850 and 940 nm, respectively, at -0.2 V. The devices are compared with standard opaque Cu top electrodes showing that the PLD top contact processing does not damage the soft layers underneath.

Results and discussion

$MA_{0.3}FA_{0.7}Pb_{0.5}Sn_{0.5}I_3$ perovskite thin films were prepared from tin reduced precursor solutions adjusting a method adapted from previous reports.[41,42] The solutions consisted of a mixture of FAI, MAI, tin iodide (SnI_2), and lead iodide (PbI_2) in a dimethylformamide (DMF) and dimethyl sulfoxide (DMSO) (3 to 1 volume ratio) solvent mixture. Anisole was used as the anti-solvent during spin-coating. A small tin foil (1 cm^2) was added to the precursor solution to prevent the unwanted oxidation of Sn^{2+} to Sn^{4+} that results in poor charge transport/extraction in optoelectronic devices.[41] As already mentioned, one of the strategies to fabricate semitransparent devices consists of using thin-film active layers coupled with transparent electrodes. To deposit thin perovskite films, low concentration precursor solutions were used. In particular, we processed films from 0.55 M solutions that resulted in 200 nm thick films. This thickness is much lower compared to those commonly used for perovskite photodetectors and solar cells, which often lie in the range of 500 to 1000 nm.[33,43] Indeed, too thin layers might impact the performance of the photodetector devices, particularly the EQE,[44] and a trade-off between performance and transparency is expected. The X-ray diffraction (XRD) characterization of a $MA_{0.3}FA_{0.7}Pb_{0.5}Sn_{0.5}I_3$ perovskite thin film is shown in Fig. 1a. The signal can be fitted considering a single cubic perovskite phase (space group $Pm\bar{3}m$) with a lattice parameter of 6.33 Å, with only a small contribution of the underlying ITO substrate.

Photodetectors using $MA_{0.3}FA_{0.7}Pb_{0.5}Sn_{0.5}I_3$ perovskite thin films as active layer were fabricated (Fig. 1b). The devices had a p–i–n configuration with the following structure: glass/ITO/PEDOT:PSS (20 nm)/$MA_{0.3}FA_{0.7}Pb_{0.5}Sn_{0.5}I_3$ (200 nm)/C_{60} (25 nm)/BCP (7 nm)/ITO (140 nm) (where PEDOT:PSS is poly(3,4-ethylenedioxythiophene) polystyrene sulfonate, C_{60} is fullerene and BCP is bathocuproine). The energy band diagram is shown in Fig. 1c. The energy levels of the perovskite layer are previously reported in literature.[45] PEDOT:PSS and C_{60}/BCP were chosen as hole and electron transport layers, respectively, as they have shown to be good candidates for these roles in Sn–Pb based solar cells.[46] Usually, ITO top electrodes are processed by ion sputtering which can easily damage any soft organic underlayers,[47] leading to increased leakage current, as well as reduced efficiency and lower lifetime of the device.[47–49] To mitigate these limitations, pulsed laser deposition (PLD) is an alternative technique that allows damage-free smooth ITO deposition on top of thin organic layers. For example, in our recent investigation, bifacial $MAPbI_3$ perovskite solar cells were fabricated by directly depositing ITO with PLD on top of the organic C_{60}/BCP electron transport layers (ETLs) with a total thickness of only 32 nm, without any protective buffer layers in between, leading to no damage to the device stack underneath and, hence, no losses in photovoltaic performance.[50] Therefore, for the fabrication of the semitransparent $MA_{0.3}FA_{0.7}Pb_{0.5}Sn_{0.5}I_3$ photodetectors investigated here, the ITO top cathode was also deposited *via* PLD directly on top of the C_{60}/BCP ETLs, using the optimized conditions previously obtained.[50] In order to prove that the deposition of the ITO top electrode was not harmful to the organic stack underneath, reference devices with a standard opaque Cu top contact (100 nm), instead of ITO, were also prepared by thermal vacuum deposition, for comparison. Although the resistivity of the PLD-ITO films is

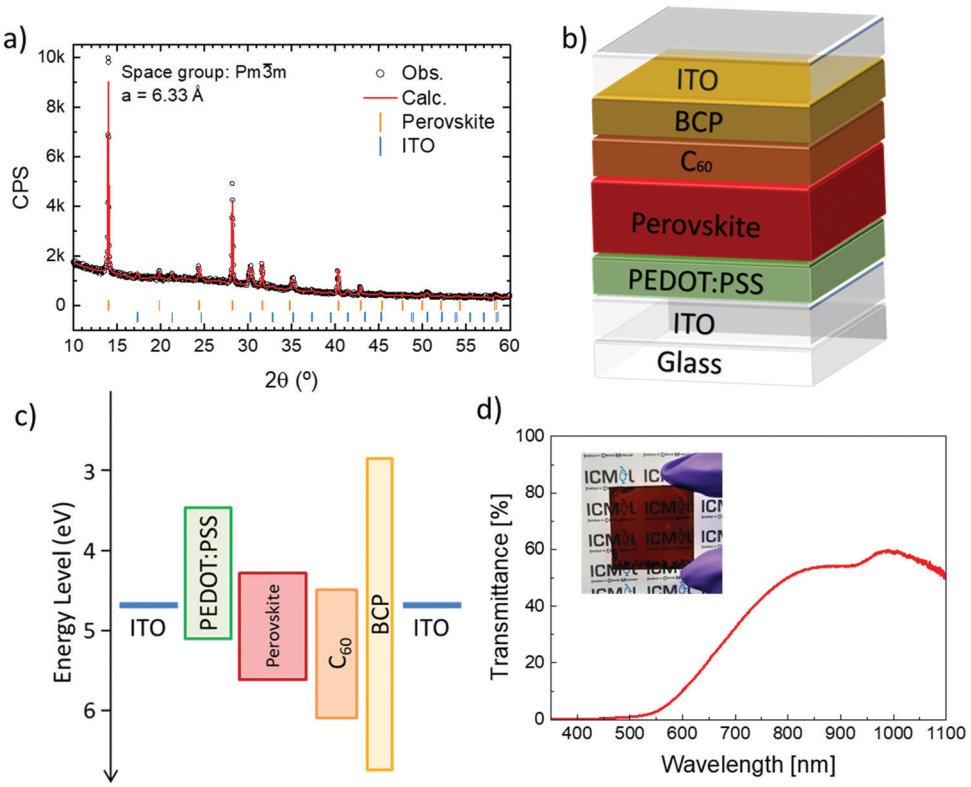

Fig. 1 (a) XRD characterization of $MA_{0.3}FA_{0.7}Pb_{0.5}Sn_{0.5}I_3$ perovskite thin films deposited on a glass/ITO substrate coated with PEDOT:PSS. Observed (experimental) intensities are marked with open circles, Le Bail fit is represented in red and Braggs' reflection for the perovskite and underlying ITO phases are indicated with vertical markers of different colors. (b) Schematic device structure of the semi-transparent perovskite photodetector. (c) Schematic energy band diagram of the photodetector. (d) Transmittance of the same full stack with a 200 nm thick active layer. Inset: Photography of the device in front of the logo of the research institute where this work was carried out.

quite low (between 0.4 to 1 mΩ cm, depending on the deposition pressure, for thicknesses of *ca.* 150 nm), it is not as low as a typical Cu film (usually around 1 μΩ cm). Therefore, to increase the conductivity of the ITO top cathode in the semitransparent devices, Au grids (100 nm thick) were thermally evaporated around the edges of the PLD-ITO cathode, but not covering the active area. This approach decreased the series resistance of devices finished with PLD-ITO from 17.4 to 4.8 mΩ cm^{-2}, within the same order of magnitude as devices using the metal top contact (~3.5 mΩ cm^{-2}).[50]

The transmittance of the full stack using 200 nm perovskite films was measured (Fig. 1d). In the visible range, the devices are opaque from 380 to almost 600 nm and their transmission starts increasing in the red region, resulting in a characteristic dark red color (Fig. 1d, inset). More importantly, in the NIR the devices are semitransparent with a transmission of over 48% (780–1100 nm wavelength range). Of particular importance are the wavelengths of 850 and 940 nm as these are wavelengths where the most commonly available commercial NIR light-emitting diodes (LEDs) emit. The whole device showed transmittance of 54% and 56% at 850 and 940 nm, respectively.

Current density *versus* voltage (*J–V*) characteristics of the devices were obtained and are shown in Fig. 2a, both in dark (blue curve) and under light (green curve). The *J–V* sweep presents almost negligible hysteresis, usually originating from halide ionic migration on the active layer.[51] The dark current density (J_D) is 1.74 × 10^{-2} mA cm^{-2} at −0.2 V. Light current density (J_{Ph}) was also measured by using a light source with a simulated AM 1.5G irradiation (100 mW cm^{-2}). The J_{Ph} is 17.7 mA cm^{-2} at −0.2 V and we do not observe nearly any voltage dependence, highlighting the efficient charge carrier extraction of these devices. The J_{Ph} is three orders of magnitude higher than the J_D (at −0.2 V). The EQE was measured at 0 V and under a constant voltage bias of −0.2, −0.4 and −0.6 V (Fig. 3b). There is virtually no voltage dependence of the EQE on the voltage, as expected form the current profile in the *J–V* curves under illumination. The devices absorb up to *ca.* 1050 nm, in line with the expected bandgap of the material (~1.22 eV),[41] with values of 23% and 13% for 850 and 940 nm, respectively. The EQE in the visible spectrum (380–780 nm) ranges from 30 to 77%. This shows that these photodetectors could be used for applications both in the visible and in the NIR range. On the other hand, for strict wavelength dependent applications, filters should be used to prevent parasitic light from reaching the active layer.[20]

We compared the performance of these devices with reference devices using a standard opaque Cu top electrode (stack: glass/ITO/PEDOT:PSS/$MA_{0.3}FA_{0.7}Pb_{0.5}Sn_{0.5}I_3$/$C_{60}$/BCP/Cu). *J–V* curves of the reference devices are shown in Fig. 2c both in dark (red curve) and under the same light conditions (green

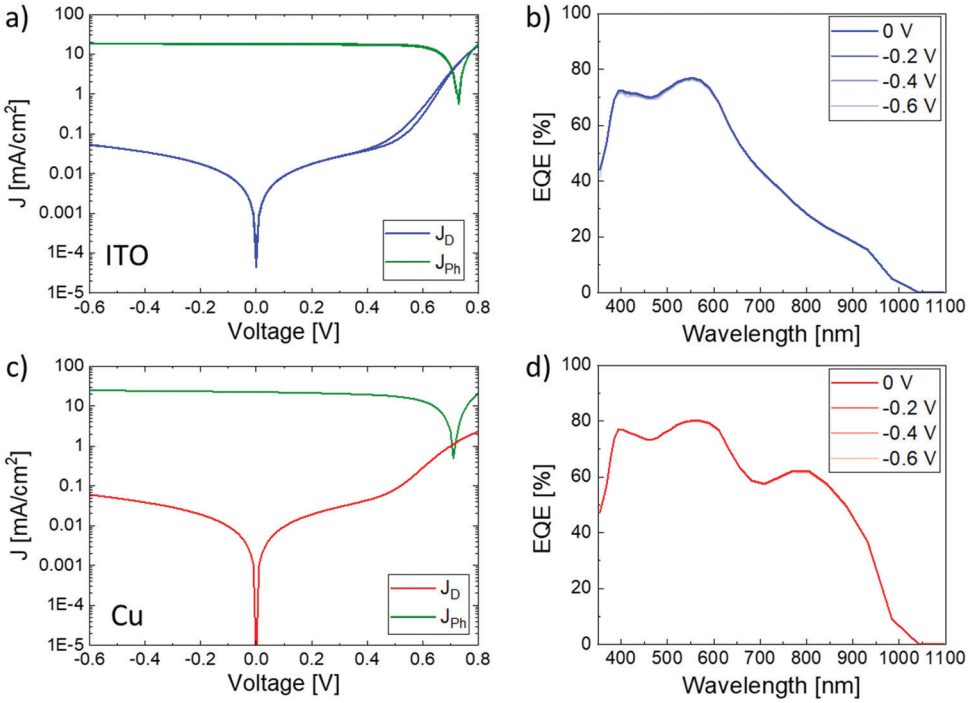

Fig. 2 (a) J–V characteristics of the semitransparent Glass/ITO/PEDOT:PSS/$MA_{0.3}FA_{0.7}Pb_{0.5}Sn_{0.5}I_3$/$C_{60}$/BCP/ITO photodetector in dark (blue curve) and under light illumination (green curve). (b) EQE spectra for the same device measured at different voltage biases (0 to −0.6 V in 0.2 V steps). (c) J–V characteristics of the standard opaque Glass/ITO/PEDOT:PSS/$MA_{0.3}FA_{0.7}Pb_{0.5}Sn_{0.5}I_3$/$C_{60}$/BCP/Cu photodetector in dark (red curve) and under light (green curve). (d) EQE spectra for the same device measured at different voltage biases (0 to −0.6 V in 0.2 V steps).

curve). The J_D and the J_{Ph} under −0.2 V are 1.92×10^{-2} mA cm^{-2} and 23.4 mA cm^{-2}, respectively. The J_D for the semitransparent and reference devices exhibits very similar values, where small differences are attributed to device-to-device variation. The shape of both curves is also very similar between the PLD-ITO and the Cu top electrode devices, indicating that the PLD processing on top of the stack has not damaged the soft layers underneath; if the PLD had damaged the underlayers, the contact/shunt resistance of the semitransparent devices would have had increased,[50] mainly affecting the slope of the J–V curves near short-circuit (from 0 to ∼0.7 V). The EQE, however, shows higher values for the reference device, all across the visible spectrum (58–80%), and at 850 nm (56%) and 940 nm (32%) (Fig. 3d). The higher EQE on the reference device is expected as the opaque electrode acts as a mirror, reflecting the non-absorbed light that crossed the device back to the active layer, where it can be reabsorbed.

The responsivity (R) is a key figure of merit that is defined as the ratio of the output photocurrent (I_{Ph}) and the input light power (P_{Ph}) at a certain wavelength and is expressed as:

$$R = \frac{I_{Ph}}{P_{Ph}} = \frac{\mathrm{EQE}}{100\%} \cdot \frac{\lambda(\mathrm{nm})}{1240} \left(\mathrm{A\,W^{-1}}\right) \qquad (1)$$

where λ is the wavelength of incident light. The R at different voltage biases (0 to −0.6 V in 0.2 V steps) of the semitransparent devices is shown in Fig. 3a. As observed for the EQE, the responsivity is also voltage independent, with values of 0.16 A W^{-1} and 0.10 A W^{-1} for 850 and 940 nm, respectively. The shot noise limited specific detectivity (D^*) is regarded as the overall figure of merit for photodetectors as it considers both the EQE and the J_D. It can be expressed as:

$$D^* = \frac{R}{\sqrt{2qJ_D}} \left(\mathrm{Jones} = \mathrm{cm}\,\sqrt{\mathrm{Hz}}\,\mathrm{W^{-1}}\right) \qquad (2)$$

where q is the elementary charge. We note that, albeit widely used in literature, this approximates the detectivity and a more accurate value can be obtained by directly measuring the noise spectral density.[43,52]

The detectivity of the semitransparent devices at −0.2, −0.4 and −0.6 V was calculated (Fig. 3b). The D^* is voltage dependent (as the J_D varies with the applied voltage) and shows values of 6.6×10^{10} and 4.2×10^{10} Jones (at −0.2 V) for 850 and 940 nm, respectively. When comparing the detectivity of our devices with semitransparent devices based on commonly-used perovskite materials such as $MAPbI_3$ or $MAPbCl_3$ we observe that previous works report higher detectivity values (in the order of 10^{12} Jones, and up to 7.3×10^{12} Jones),[38,53] albeit these devices can absorb only in the UV and visible ranges, hindering their applicability in the NIR. An alternative to our approach would be to add a PbSe quantum dot layer on top of the $MAPbI_3$ layer. In this way absorption can be enhanced up to 2600 nm, at the cost of a more complex device structure.[40]

Both R and D^* were also determined for the reference opaque devices (Fig. 3c and d). In both cases, the values were

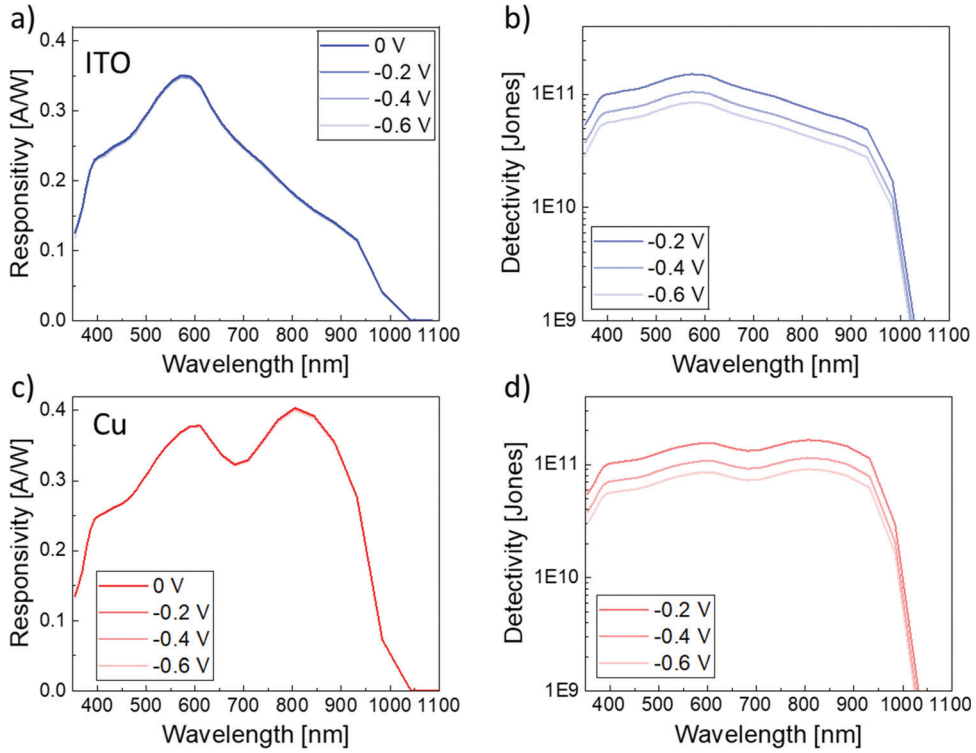

Fig. 3 (a) Responsivity (R) as a function of wavelength of the semitransparent Glass/ITO/PEDOT:PSS/$MA_{0.3}FA_{0.7}Pb_{0.5}Sn_{0.5}I_3$/$C_{60}$/BCP/ITO photodetector at different voltage biases (0 to −0.6 V in 0.2 V steps). (b) Detectivity (D^*) as a function of wavelength for the same device measured at different voltage biases (−0.2 V to −0.6 V in 0.2 V steps). (c) R as a function of wavelength of the standard opaque Glass/ITO/PEDOT:PSS/$MA_{0.3}FA_{0.7}Pb_{0.5}Sn_{0.5}I_3$/$C_{60}$/BCP/Cu photodetector at different voltage biases (0 to −0.6 V in 0.2 V steps). (d) D^* as a function of wavelength for the same device measured at different voltage biases (−0.2 V to −0.6 V in 0.2 V steps).

higher (at −0.2 V) than the semitransparent devices with R of 0.39 and 0.24 A W^{-1} and D^* of 1.6×10^{11} and 9.2×10^{10} Jones (at −0.2 V) for 850 and 940 nm, respectively. Again, the higher values for the reference devices are related to the higher EQE exhibited by these devices due to the use of an opaque reflecting top contact. Therefore, it is difficult to directly compare the R and D^* of the semitransparent device with other NIR perovskite photodetector works reported in the literature where an opaque reflective top contact is used.[29] In order to improve the detectivity, J_D has to be reduced, as EQE will always be limited by the thickness of the devices (due to the trade-off between EQE and transparency). Recently it has been shown that the origin of the dark current in perovskite photodetectors is due to the interfacial energy offset between the perovskite and the electron blocking layer (EBL).[45] Carefully choosing an EBL with a lower highest occupied molecular orbital (HOMO) than PEDOT:PSS (*e.g.* poly(4-butyl-*N*,*N*-diphenylaniline) (poly-TPD)) could further improve the J_D of these devices and will be subject of further study. Other strategies, such as using an edge cover layer, covering edges and corners of the pixels, have also been shown to be effective.[43]

Finally, the linearity of the semitransparent devices was examined at −0.6 V illuminating from both top and bottom sides. Fig. 4 shows the J_{Ph} as a function of the incident light intensity. In both cases the device behaves linearly in the 100 to 1 mW cm^{-2} light intensity range (R-square of 0.997 and 0.998 for top and bottom illumination, respectively), deviating at lower values due to the noise current of the device.[54] These results indicate that the device has the same response irrespectively from the direction of the illumination and could effectively be used for applications where a high transparency (both in the visible and in the NIR) is needed, or as bifacial devices in a range of lighting conditions.

Conclusions

We have reported a NIR semitransparent photodetector based on a $MA_{0.3}FA_{0.7}Pb_{0.5}Sn_{0.5}I_3$ perovskite active layer with a full stack transmission of over 48% in the NIR (between 780 and 1100 nm). To achieve this, we have fabricated thin perovskite layers (200 nm) sandwiched between two semitransparent ITO electrodes. The top electrode was deposited *via* PLD, which is a soft deposition method harmless to the underlying organic stack. The photodetectors showed a dark current of 1.74×10^{-2} mA cm^{-2} (at −0.2 V), EQEs of 23% and 13% and D^* of 6.6×10^{10} and 4.2×10^{10} Jones (at −0.2 V) for 850 and 940 nm, respectively. No difference in the response was observed when illuminating from either side of the device at different light intensities. These findings could lead to the

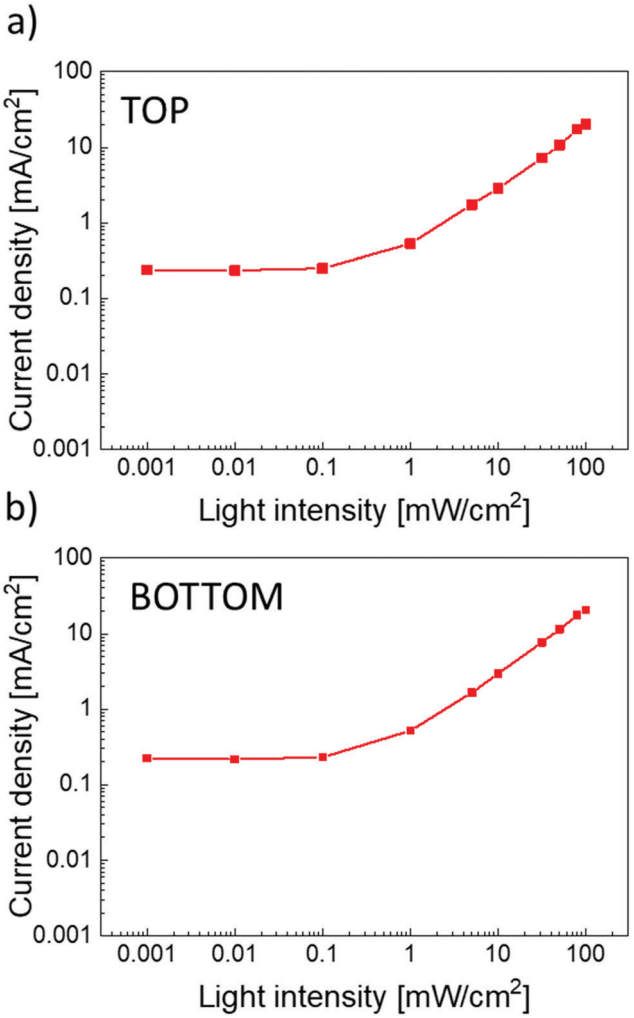

Fig. 4 Linearity (current density *vs.* light power) of the semitransparent (ITO top contact) $MA_{0.3}FA_{0.7}Pb_{0.5}Sn_{0.5}I_3$ perovskite photodetector illuminated from the (a) top and (b) bottom.

development of novel NIR semitransparent perovskite photodetectors that could open new application possibilities for this technology.

Experimental section

Materials

PEDOT:PSS (Al 4083) was purchased from Heraeus Clevios. Dimethylformamide and dimethyl sulfoxide were purchased from VWR. Sn foil, anisole and SnF_2 were purchased from Sigma Aldrich. Fullerene (C_{60}) was purchased from Merck KGaA. CH_3NH_3I (MAI), $CHNH_2NH_2I$ (FAI) and bathocuproine (BCP) were purchased from Luminescence Technology Corp. Tin iodide (SnI_2) and lead iodide (PbI_2) were purchased from Alfa Aesar.

Device fabrication

ITO-coated glass substrates were subsequently cleaned with soap, water and isopropanol in an ultrasonic bath, followed by a 20 min UV-ozone treatment. PEDOT:PSS was filtered with a 0.45 μm polypropylene filter, then spin-coated on the ITO-coated glass substrates (4000 rpm for 30 seconds). Subsequently, the substrates were annealed at 150 °C for 10 minutes. For the preparation of the perovskite precursor molar ratios of 0.385 MAI, 0.165 FAI, 0.275 PbI_2, 0.275 SnI_2 and 0.0275 SnF_2 (10% of SnI_2 molar ratio) were mixed in DMF : DMSO (3 : 1) with a resulting 0.55 M concentration. In order to suppress the Sn oxidation, a tin foil (1 cm^2) was inserted in the precursor for 10 minutes. The precursor was filtered with a 0.45 μm polytetrafluoroethylene filter and spin-coated at 1000 rpm for 10 seconds and 4000 rpm for 40 seconds. The anisole was dropped dynamically on the substrate. Sequentially, the samples were annealed at 100 °C for 10 minutes. Finally, 140 nm of ITO were deposited by PLD using a Solmates' large area PLD 200 mm system coupled to a Lightmachinery's IPEX-700 KrF excimer laser (λ = 248 nm, with a repetition rate of 25 Hz and a fluence of 1.5–1.7 J cm^{-2}). The source material for ITO deposition was a Sn:In_2O_3 ceramic target with 2 : 98 wt% and the chamber pressure was set at 0.033 mbar, with an O_2 partial pressure of 0.007 mbar controlled by a constant injection of an oxygen/argon gas mix, as optimized in our previous paper.[50] Shadow masks were used during the ITO deposition to obtain a final active area of 0.06 cm^2. The Au grids (100 nm thick) at the side of the PLT-ITO cathodes were thermally evaporated. The devices were prepared in an inert atmosphere inside the glovebox and characterized outside. Prior to the characterization, the stacks were encapsulated using atomic layer deposition for the deposition of a transparent Al_2O_3 (30 nm) film at 40 °C to prevent possible degradation from ambient conditions.[55]

X-ray diffraction

The patterns were collected in Bragg–Brentano geometry on an Empyrean PANalytical powder diffractometer with a copper anode operated at 45 kV and 40 mA. Further analysis including Le Bail fits were performed with Fullprof software.

Optical and optoelectronic characterization

The transmittance was measured with an Avantes AvaLight-DS-S-BAL deuterium halogen light source and an Avantes AvaSpec-2048L spectrometer. The *J–V* curves of the devices were measured with a Keithley 2612A SourceMeter under dark and illuminated with a Wavelabs Sinus 70 LED solar simulator (AM 1.5G irradiation (100 mW cm^{-2})) and recorded using a custom LabVIEW program. A step of 0.01 voltage was used. The light intensity was calibrated before every measurement using a calibrated Si reference diode. Intensity dependent data was carried out by measuring *J–V* curves in the same system using neutral density filters of decreasing optical density. The external quantum efficiency (EQE) was measured using a Quartz-Tungsten-Halogen lamp (Newport Apex 2-QTH) source, a monochromator (Newport CS130-USB-3-MC), a chopper (at 279 Hz) and a focusing lens. The device current was measured as a function of energy using a lock-in amplifier (Stanford Research Systems SR830) and recorded using a custom LabVIEW program. The system was calibrated, and the solar

spectrum mismatch was corrected using a calibrated Si reference cell.

Conflicts of interest

The authors have no conflict of interest to declare.

Acknowledgements

We acknowledge support from the Comunitat Valenciana (PROMETEU/2020/077, APOSTD/2021/368), the Spanish Ministry of Science and Innovation (MCIN) and the Spanish State Research Agency (AEI): projects MAT2017-88821-R and RTI2018-095362-A-I00 funded by MCIN/AEI/10.13039/501100011033 and by "ERDF A way of making Europe"; project PCI2020-112084 funded by MCIN/AEI/10.13039/501100011033 and by the "European Union NextGenerationEU/PRTR"; grant RYC-2016-21316 and PRE2018-084619 funded by MCIN/AEI/10.13039/501100011033 and by "ESF Investing in your future".

References

1 A. Rogalski, J. Antoszewski and L. Faraone, *J. Appl. Phys.*, 2009, **105**, 91101.
2 E. K. Bolton, G. S. Sayler, D. E. Nivens, J. M. Rochelle, S. Ripp and M. L. Simpson, *Sens. Actuators, BSens. Actuators, B*, 2002, **85**, 179–185.
3 S. Kim, Y. T. Lim, E. G. Soltesz, A. M. De Grand, J. Lee, A. Nakayama, J. A. Parker, T. Mihaljevic, R. G. Laurence, D. M. Dor, L. H. Cohn, M. G. Bawendi and J. V. Frangioni, *Nat. Biotechnol.*, 2004, **22**, 93–97.
4 D. Tordera, B. Peeters, H. B. Akkerman, A. J.-J. M. van Breemen, J. Maas, S. Shanmugam, A. J. Kronemeijer and G. H. Gelinck, *Adv. Mater. Technol.*, 2019, **4**, 1900651.
5 T. Yokota, T. Nakamura, H. Kato, M. Mochizuki, M. Tada, M. Uchida, S. Lee, M. Koizumi, W. Yukita, A. Takimoto and T. Someya, *Nat. Electron.*, 2020, **3**, 113–121.
6 T. Yokota, P. Zalar, M. Kaltenbrunner, H. Jinno, N. Matsuhisa, H. Kitanosako, Y. Tachibana, W. Yukita, M. Koizumi and T. Someya, *Sci. Adv.*, 2016, **2**, e1501856.
7 D. C. Ng, T. Tokuda, A. Yamamoto, M. Matsuo, M. Nunoshita, H. Tamura, Y. Ishikawa, S. Shiosaka and J. Ohta, *Sens. Actuators, B*, 2006, **119**, 262–274.
8 C.-H. Chen, C.-F. Lin, K.-H. Wang, H.-C. Liu, H.-W. Zan, H.-F. Meng, W. Hortschitz, H. Steiner, A. Kainz and T. Sauter, *Org. Electron.*, 2017, **49**, 305–312.
9 C. Harbeck, R. Faurie and T. Scheper, *Anal. Chim. Acta*, 2004, **501**, 249–253.
10 L. Rey-Barroso, F. J. Burgos-Fernández, X. Delpueyo, M. Ares, S. Royo, J. Malvehy, S. Puig and M. Vilaseca, *Sensors*, 2018, **18**, 1441.
11 H. Akkerman, B. Peeters, A. van Breemen, S. Shanmugam, L. Ugalde Lopez, D. Tordera, R. van de Ketterij, E. Delvitto, R. Verbeek, P. Malinowski, T.-H. Ke, F. De Roose, L. Moreno Hagelsieb, I. Katsouras, A. J. Kronemeijer, E. Meulenkamp and G. Gelinck, *J. Soc. Inf. Disp.*, 2021, **29**, 935–947.
12 P. E. Malinowski, A. Nakamura, D. Janssen, Y. Kamochi, I. Koyama, Y. Iwai, A. Stefaniuk, E. Wilenska, C. Salas Redondo, D. Cheyns, S. Steudel and P. Heremans, *Org. Electron.*, 2014, **15**, 2355–2359.
13 A. Colsmann, A. Puetz, A. Bauer, J. Hanisch, E. Ahlswede and U. Lemmer, *Adv. Energy Mater.*, 2011, **1**, 599–603.
14 Y. Xie, R. Xia, T. Li, L. Ye, X. Zhan, H. L. Yip and Y. Sun, *Small Methods*, 2019, **3**, 1900424.
15 V. V. Brus, J. Lee, B. R. Luginbuhl, S. J. Ko, G. C. Bazan and T. Q. Nguyen, *Adv. Mater.*, 2019, **31**, 1900904.
16 H. Schmidt, H. Flügge, T. Winkler, T. Bülow, T. Riedl and W. Kowalsky, *Appl. Phys. Lett.*, 2009, **94**, 243302.
17 D. Tordera, A. J.-J. M. van Breemen, A. J. Kronemeijer, J.-L. van der Steen, B. Peeters, S. Shanmugan, H. B. Akkerman and G. H. Gelinck, *Organic Flexible Electronics*, Elsevier, 2021, pp. 575–597.
18 J. Kim, S.-M. Kwon, Y. K. Kang, Y.-H. Kim, M.-J. Lee, K. Han, A. Facchetti, M.-G. Kim and S. K. Park, *Sci. Adv.*, 2019, **5**, eaax8801.
19 S. Tong, H. Wu, C. Zhang, S. Li, C. Wang, J. Shen, S. Xiao, J. He, J. Yang, J. Sun and Y. Gao, *Org. Electron.*, 2017, **49**, 347–354.
20 D. Tordera, B. Peeters, E. Delvitto, S. Shanmugam, J. Maas, J. de Riet, R. Verbeek, R. van de Laar, T. Bel, G. Haas, L. Ugalde, A. van Breemen, I. Katsouras, A. J. Kronemeijer, H. Akkerman, E. Meulenkamp and G. Gelinck, *J. Soc. Inf. Disp.*, 2020, **28**, 381–391.
21 V. M. Goldschmidt, *Naturwissenschaften*, 1926, **14**, 477–485.
22 A. Kojima, K. Teshima, Y. Shirai and T. Miyasaka, *J. Am. Chem. Soc.*, 2009, **131**, 6050–6051.
23 X. Peng, J. Yuan, S. Shen, M. Gao, A. S.-R. Chesman, H. Yin, J. Cheng, Q. Zhang and D. Angmo, *Adv. Funct. Mater.*, 2017, **27**, 1703704.
24 L. Gil-Escrig, C. Momblona, M. G. La-Placa, P. P. Boix, M. Sessolo and H. J. Bolink, *Adv. Energy Mater.*, 2018, **8**, 1703506.
25 N. J. Jeon, J. H. Noh, W. S. Yang, Y. C. Kim, S. Ryu, J. Seo and S. Il Seok, *Nature*, 2015, **517**, 476–480.
26 J. Jeong, M. Kim, J. Seo, H. Lu, P. Ahlawat, A. Mishra, Y. Yang, M. A. Hope, F. T. Eickemeyer, M. Kim, Y. J. Yoon, I. W. Choi, B. P. Darwich, S. J. Choi, Y. Jo, J. H. Lee, B. Walker, S. M. Zakeeruddin, L. Emsley, U. Rothlisberger, A. Hagfeldt, D. S. Kim, M. Grätzel and J. Y. Kim, *Nature*, 2021, **592**, 381–385.
27 Y. Wang, D. Yang, X. Zhou, S. M. Alshehri, T. Ahamad, A. Vadim and D. Ma, *Org. Electron.*, 2017, **42**, 203–208.
28 T. Hellmann, C. Das, T. Abzieher, J. A. Schwenzer, M. Wussler, R. Dachauer, U. W. Paetzold, W. Jaegermann and T. Mayer, *Adv. Energy Mater.*, 2020, **10**, 2002129.
29 J. Miao and F. Zhang, *J. Mater. Chem. C*, 2019, **7**, 1741–1791.
30 F. P. de Arquer, X. Gong, R. P. Sabatini, M. Liu, G.-H. Kim, B. R. Sutherland, O. Voznyy, J. Xu, Y. Pang, S. Hoogland, D. Sinton and E. Sargent, *Nat. Commun.*, 2017, **8**, 14757.
31 C. Liu, K. Wang, P. Du, E. Wang, X. Gong and A. J. Heeger, *Nanoscale*, 2015, **7**, 16460–16469.
32 A. Waleed, M. M. Tavakoli, L. Gu, Z. Wang, D. Zhang, A. Manikandan, Q. Zhang, R. Zhang, Y.-L. Chueh and Z. Fan, *Nano Lett.*, 2017, **17**, 523–530.

33 Y. Zhao, C. Li, J. Jiang, B. Wang and L. Shen, *Small*, 2020, **16**, 2001534.
34 H. L. Zhu, H. Lin, Z. Song, Z. Wang, F. Ye, H. Zhang, W. J. Yin, Y. Yan and W. C.-H. Choy, *ACS Nano*, 2019, **13**, 11800–11808.
35 Y. Ogomi, A. Morita, S. Tsukamoto, T. Saitho, N. Fujikawa, Q. Shen, T. Toyoda, K. Yoshino, S. S. Pandey, T. Ma and S. Hayase, *J. Phys. Chem. Lett.*, 2014, **5**, 1004–1011.
36 F. Hao, C. C. Stoumpos, R. P.-H. Chang and M. G. Kanatzidis, *J. Am. Chem. Soc.*, 2014, **136**, 8094–8099.
37 Y. Wang, C. Chen, T. Zou, L. Yan, C. Liu, X. Du, S. Zhang and H. Zhou, *Adv. Mater. Technol.*, 2020, **5**, 1900752.
38 F. Cao, W. Tian, M. Wang, H. Cao and L. Li, *Adv. Funct. Mater.*, 2019, **29**, 1901280.
39 R. Xu, L. Min, Z. Qi, X. Zhang, J. Jian, Y. Ji, F. Qian, J. Fan, C. Kan, H. Wang, W. Tian, L. Li, W. Li and H. Yang, *ACS Appl. Mater. Interfaces*, 2020, **12**, 16462–16468.
40 T. Zhu, Y. Yang, L. Zheng, L. Liu, M. L. Becker and X. Gong, *Adv. Funct. Mater.*, 2020, **30**, 1909487.
41 R. Lin, K. Xiao, Z. Qin, Q. Han, C. Zhang, M. Wei, M. I. Saidaminov, Y. Gao, J. Xu, M. Xiao, A. Li, J. Zhu, E. H. Sargent and H. Tan, *Nat. Energy*, 2019, **4**, 864–873.
42 K. Xiao, R. Lin, Q. Han, Y. Hou, Z. Qin, H. T. Nguyen, J. Wen, M. Wei, V. Yeddu, M. I. Saidaminov, Y. Gao, X. Luo, Y. Wang, H. Gao, C. Zhang, J. Xu, J. Zhu, E. H. Sargent and H. Tan, *Nat. Energy*, 2020, **5**, 870–880.
43 A. J.-J. M. van Breemen, R. Ollearo, S. Shanmugam, B. Peeters, L. C.-J. M. Peters, R. L. van de Ketterij, I. Katsouras, H. B. Akkerman, C. H. Frijters, F. Di Giacomo, S. Veenstra, R. Andriessen, R. A.-J. Janssen, E. A. Meulenkamp and G. H. Gelinck, *Nat. Electron.*, 2021, **4**, 818–826.
44 W. Wang, D. Zhao, F. Zhang, L. Li, M. Du, C. Wang, Y. Yu, Q. Huang, M. Zhang, L. Li, J. Miao, Z. Lou, G. Shen, Y. Fang and Y. Yan, *Adv. Funct. Mater.*, 2017, **27**, 1703953.
45 R. Ollearo, J. Wang, M. J. Dyson, C. H.-L. Weijtens, M. Fattori, B. T. van Gorkom, A. J.-J. M. van Breemen, S. C.-J. Meskers, R. A.-J. Janssen and G. H. Gelinck, *Nat. Commun.*, 2021, **12**, 7277.
46 D. Zhao, Y. Yu, C. Wang, W. Liao, N. Shrestha, C. R. Grice, A. J. Cimaroli, L. Guan, R. J. Ellingson, K. Zhu, X. Zhao, R. G. Xiong and Y. Yan, *Nat. Energy*, 2017, **2**, 17018.
47 E. Aydin, C. Altinkaya, Y. Smirnov, M. A. Yaqin, K. P.-S. Zanoni, A. Paliwal, Y. Firdaus, T. G. Allen, T. D. Anthopoulos, H. J. Bolink, M. Morales-Masis and S. De Wolf, *Matter*, 2021, **4**, 3549–3584.
48 H. Kanda, A. Uzum, A. K. Baranwal, T. A.-N. Peiris, T. Umeyama, H. Imahori, H. Segawa, T. Miyasaka and S. Ito, *J. Phys. Chem. C*, 2016, **120**, 28441–28447.
49 Q. H. Fan, M. Deng, X. Liao and X. Deng, *J. Appl. Phys.*, 2009, **105**, 33304.
50 K. P.-S. Zanoni, A. Paliwal, M. A. Hernández-Fenollosa, P.-A. Repecaud, M. Morales-Masis and H. J. Bolink, *Adv. Mater. Technol.*, 2022, 2101747.
51 D.-H. Kang and N.-G. Park, *Adv. Mater.*, 2019, **31**, 1805214.
52 Y. Fang, A. Armin, P. Meredith and J. Huang, *Nat. Photonics*, 2019, **13**, 1–4.
53 V. Adinolfi, O. Ouellette, M. I. Saidaminov, G. Walters, A. L. Abdelhady, O. M. Bakr and E. H. Sargent, *Adv. Mater.*, 2016, **28**, 7264–7268.
54 R. D. Jansen-van Vuuren, A. Armin, A. K. Pandey, P. L. Burn and P. Meredith, *Adv. Mater.*, 2016, **28**, 4766–4802.
55 I. C. Kaya, K. P.-S. Zanoni, F. Palazon, M. Sessolo, H. Akyildiz, S. Sonmezoglu and H. J. Bolink, *Adv. Energy Sustainable Res.*, 2021, **2**, 2000065.